Protectively Coated Phosphors for Flat Panel FED Devices

J.S. Sanghera, G. Villalobos, S.S. Bayya, and
I.D. Aggarwal
Optical Sciences Division

The Problem: Cathode ray tube (CRT)-based displays operate on the principle that accelerated electrons excite phosphor particles on a screen, which subsequently emit visible light. However, there is a worldwide effort to reduce the bulkiness of the CRT displays. One approach is based on field emission display (FED) technology in which the electron gun in the CRT is replaced with a miniature field emitter (Fig. 1). Unfortunately, the zinc sulfide-based phosphors developed for use in CRTs are not optimized for use in the FED environment. FED devices work at much lower accelerating voltages, and therefore, driving currents have to be greatly increased to maintain adequate brightness. Surface degradation of the phosphor occurs due to reaction with residual gases in the vacuum, and this is exacerbated by the higher current density. This degradation leads to decreased brightness (aging). In addition, the volatile by-products from the phosphor surface cause poisoning of the field emitter tips. Consequently, the FED device ages at an accelerated rate.

The NRL Solution: Worldwide attempts to produce new, durable, and high-efficiency phosphors have not been successful. The alternative approach used by NRL requires that the phosphor particles be hermetically coated with a protective film. The film protects the surface of the phosphor particle and prevents attack by residual gases in the FED environment. Our approach allows existing sulfide-based phosphors to be used.

Technical Approach: We selected silica as the coating material because it is passive and does not react with zinc sulfide. Traditional "bucket chemistry" approaches produce particulates of silica distributed sporadically on the surface of the phosphor particles as well as dispersed throughout as a secondary phase (Fig. 2(a)). However, we are able to obtain uniform and smooth coatings on the phosphor particles by spraying a slurry containing the phosphor particles and the dissolved coating precursor (Fig. 2 (b)). The spray system consists of an ultrasonic atomizer, a 3-m-long drying column, and a cyclone separator. The key is to prevent gelation or precipitation of the silica before spraying so that the phosphor particles can be individually coated with silica during flight. After spraying, the coated phosphor is heat-treated to remove residual organics and to further densify the coating. The thickness of the film is controlled by varying the coating precursor concentration and ratio of phosphor particles, but typically we apply a 10-nm-thick coating of silica. The coating integrity is confirmed using a simple HCl acid test.

Results: The efficiency, chromaticity, and aging characteristics are important properties that need to be measured if the coated phosphor is to be commercially used in an FED device. The efficiency and chromaticity of the coated phosphors are comparable to the uncoated phosphors. More importantly, the

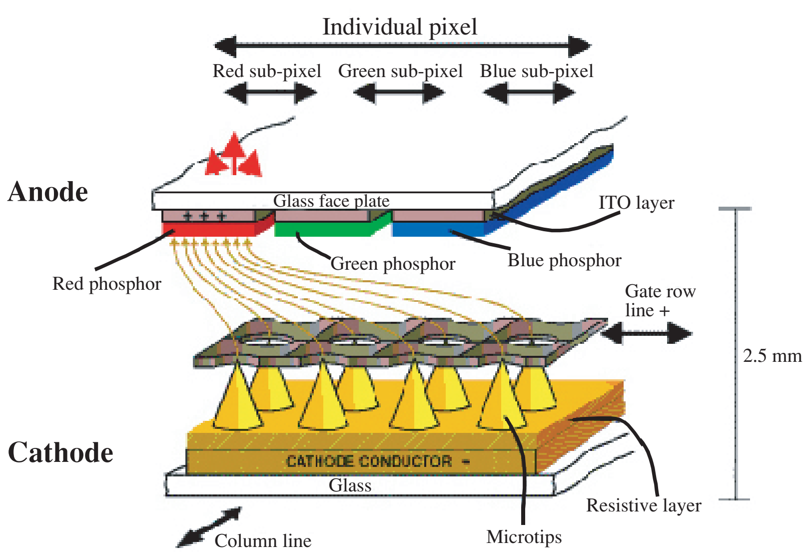

FIGURE 1
FED device.

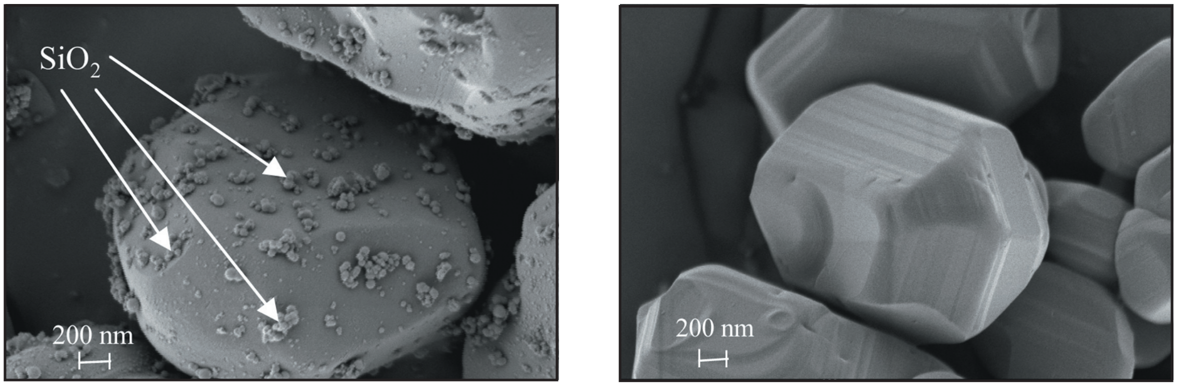

(a)

(b)

FIGURE 2
(a) Traditional "bucket chemistry"approach highlighting secondary phase particles of SiO_2 on ZnS:Ag phosphor particles, (b) a uniform and smooth coating of SiO_2 (10-nm-thck) on ZnS:Ag phosphor particles using the NRL-developed spray coating technique.

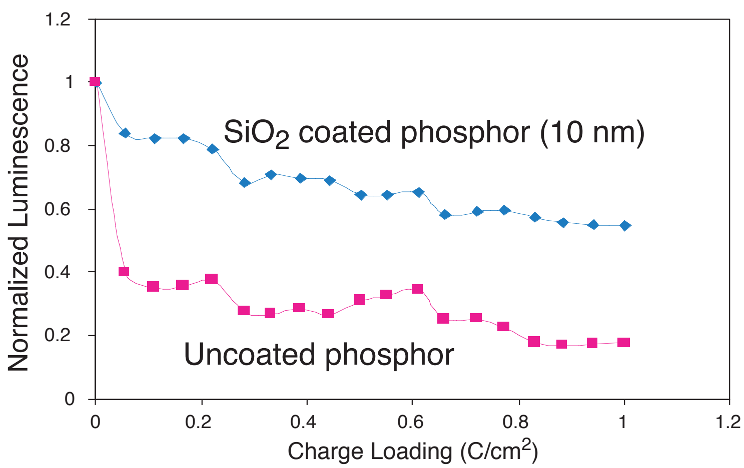

FIGURE 3
Normalized aging curves for coated and uncoated ZnS:Ag phosphor.

coating needs to provide protection against aging. Figure 3 shows the results for the accelerated aging experiments. The goal was to maintain 50% of the original brightness after charge loading of 1 C/cm^2. The coated phosphor brightness decreases to only 60% of its original value, which is acceptable, compared with 18% for the uncoated phosphor. These results generated significant industry interest, and the spray coating process was successfully scaled up to provide larger quantities of coated phosphor to commercial vendors for testing and evaluation in their proprietary FED environments.

Future: The results so far appear to be very encouraging and should result in licensing our patents and technology to industry. Although the coatings are uniform and smooth, we have identified nanoscale porosity in the coating, which probably leads to the small amount of aging observed in the coated phosphors. Even though our coated phosphor is acceptable for FED applications, we are now developing a double spraying process, whereby the coated phosphor is resprayed to fill in the initial nanoporosity. This could potentially result in no aging. These double-coated phosphors will be available for industrial evaluation in the near future.

The spray coating process is very versatile. It has also been used to apply MgO, indium tin oxide, sodium phosphate, and alumina coatings and can be used for organic coatings as well. These and other coatings will be exploited in the future in new programs.

Acknowledgments: We acknowledge the efforts of Fritz Miklos (SF Associates) for assisting in the spray coating scale-up process; Lauren Shea (Sandia National Laboratories) for the aging measurements; industrial collaborations with Candescent Corp., Lumileds (Hewlett Packard—Philips), Gemfire, and Motorola; and Bruce Gnade (DARPA) for financial support and helpful discussions.

[Sponsored by NRL and DARPA]

Scanning Nanomechanics

K.J. Wahl,[1] S.A. Syed Asif,[2] and
R.J. Colton[1]
[1]*Chemistry Division*
[2]*Present address: Hysitron, Inc.*

Introduction: The invention of the scanning tunneling microscope (STM) and atomic force microscope (AFM) in the 1980s has led to rapid commercialization of microscopes that image surfaces with atomic resolution. As a result, our materials analyses capabilities at the nanoscale have expanded enormously and now include magnetic, dielectric, tribological, electrochemical, thermal, and mechanical properties. However, despite the many advances in commercially available instrumentation, dynamic mechanical analysis at this scale has been an elusive goal. To resolve this problem, we have developed a hybrid nanoindentation system capable of measuring quantitatively dynamic materials properties. The output of this instrument can also be in the form of an image or map of mechanical response or property (e.g., stiffness, modulus). This article describes NRL's recent advances in mapping dynamic mechanical properties.

Method: High-resolution mapping of mechanical properties is possible through the use of a "hybrid" nanoindenter that combines depth-sensing nanoindentation with an AFM. This combination enables quantitative nanomechanical properties analyses with nanometer-scale positioning and topographical mapping. These scanning and positioning capabilities allow investigations of materials and structures (e.g., composites, nanostructured materials, lithographic patterns, or micro-electromechanical systems (MEMS)) that have features below the optical limit.

In an indentation experiment, mechanical properties are evaluated by using a rigid probe of well-defined shape (e.g., a pyramid or sphere) to elastically or plastically deform a sample while monitoring the load and displacement response. We have improved the sensitivity of the hybrid nanoindenter by introducing a small sinusoidal component to the indentation force and detecting the displacement signal with a lock-in amplifier.[1] The result is a dynamic measurement of contact stiffness that is related to both the contact size and elastic properties of the contacting materials.

Two significant capabilities arise from these dynamic stiffness measurements. First, by scanning the sample under the oscillating probe at low loads (elastically), a two-dimensional map of the dynamic stiffness of the sample can be obtained.[2] Second, by varying the frequency of the oscillations, we can investigate dynamic mechanical properties inherent in many polymers and biomaterials. Figure 4 is a schematic of the instrument.

Modulus Mapping of a Composite Material: Figure 5(a) shows a 10×10 µm image mapping the elastic (storage) modulus of a carbon fiber-epoxy composite. Contrast in the image, as well as the rendered height, correspond directly to modulus with lighter regions having higher modulus. Figure 5 was obtained by applying a Hertzian contact model, describing the contact of a sphere against a flat, to the measured contact stiffness during the dynamic imaging of the composite. When the probe radius R, applied load P, and measured contact stiffness K are known, the reduced elastic modulus E^* can be directly calculated, pixel by pixel, from the contact stiffness image data obtained during scanning:

$$E^* = \sqrt{\frac{K^3}{6PR}}. \qquad (1)$$

Figure 5(b) shows a cross section through the center of the image of the elastic modulus. The image shows that the center of the carbon fiber has a lower modulus than the periphery, while the epoxy has a substantially lower modulus than the fiber.

The elastic modulus values obtained during the modulus mapping experiment were consistent with measured values from standard indentation experiments. More importantly, the low loads used during modulus mapping minimized the contact area between the probe and sample, thereby increasing the lateral resolution of the technique.

Imaging the Frequency-Dependent Properties of Polymers: Stiffness images can be acquired over a range of frequencies up to ~250 Hz, allowing investigation of dynamic mechanical properties of viscoelastic materials. Figure 6(a) and (b) shows two contact stiffness images of a cross section of a layered polystyrene (PS) sample, with alternating low (PS1) and high (PS2) molecular weights. The lighter regions in the images correspond to higher contact stiffness. The two images were taken from the same region of the sample while oscillating the probe at 105 and 200 Hz, respectively. At 200 Hz, the image contrast is reversed, indicating a strong frequency-dependent response of the two PS materials within this frequency range.

This image contrast reversal reflects a change in contact stiffness caused by the frequency-dependent dissipative properties of the two polymers. Figure 6(c) plots the dynamic compliance (1/stiffness) of the nanoindenter probe in contact with the two polymers

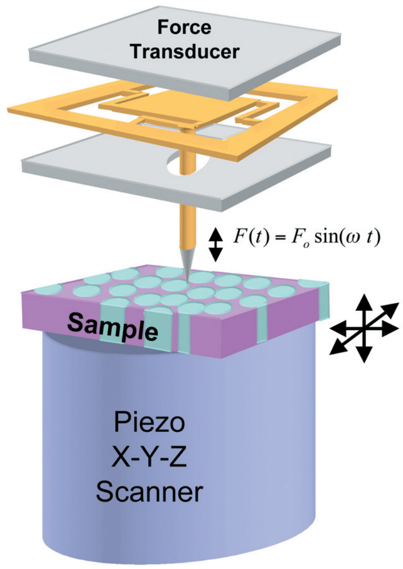

FIGURE 4
"Hybrid" scanning nanoindenter. The load-displacement response of a probe attached to a movable plate is actuated electrostatically to apply force; the displacement response is monitored by capacitive techniques. Sample *x-y* positioning and scanning are accomplished through a piezo-tube scanner.

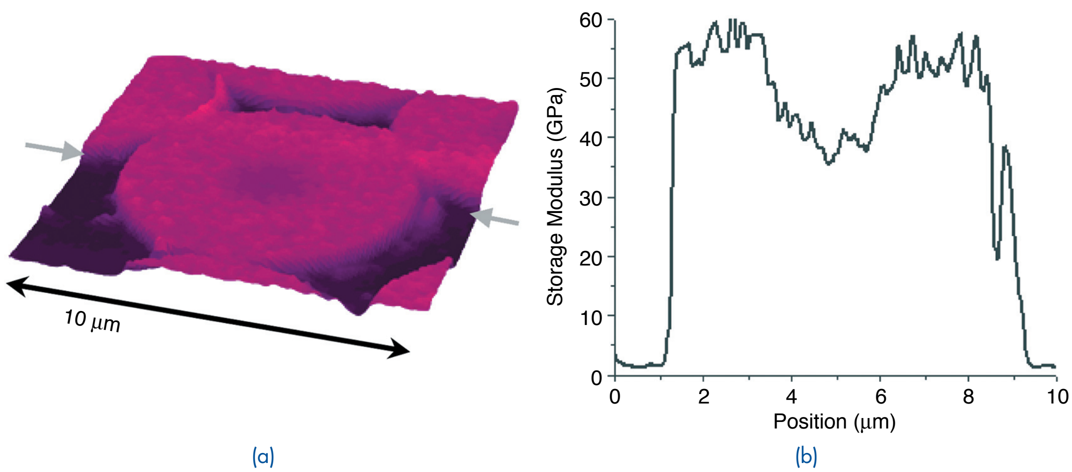

FIGURE 5
(a) Two-dimensional map of the elastic modulus of a carbon fiber-epoxy composite material. Brighter regions of the image correspond to higher modulus. (b) Cross-section line scan through the center of the image (marked by arrows in (a)) shows the storage modulus in the epoxy and the modulus gradient at the center of the fiber.

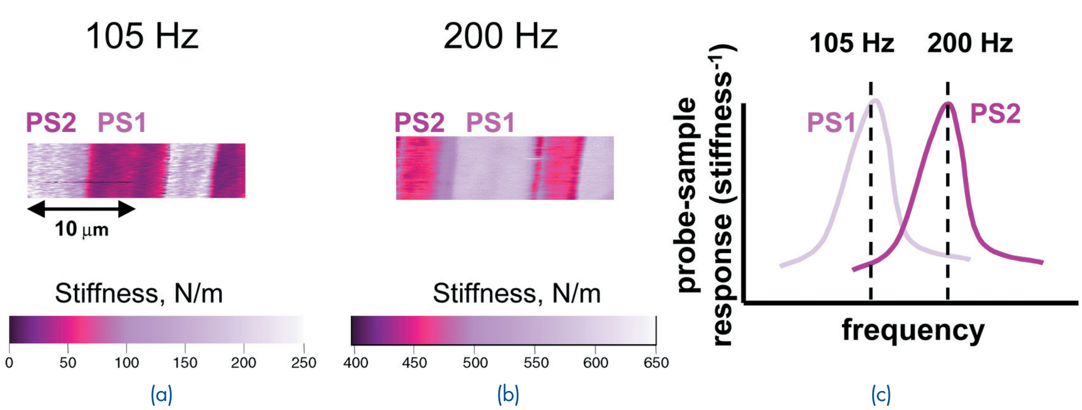

FIGURE 6
Stiffness images of alternating layers of polystyrene (PS) of two molecular weights at (a) 105 Hz and (b) 200 Hz. The contrast is due to frequency-dependent mechanical response of the polymers. The probe-sample response (1/stiffness) as a function of frequency shown in (c) is consistent with the stiffness images.

as a function of frequency. This plot shows that the stiffness of PS1 should be lower than PS2 at 105 Hz, but higher than PS2 at 200 Hz. Because the compliance maxima (and equivalent stiffness minima) of the polymers occur near 100 Hz for PS1 and near 200 Hz for PS2, dynamic imaging at these two frequencies results in a stiffness contrast reversal due to the change in relative compliance between the polymers.

Summary: We have demonstrated the quantitative mapping of dynamic contact stiffness and elastic modulus with submicron spatial resolution. This new "scanning nanomechanics" technique is capable of mapping elastic and visco-elastic response and is an ideal tool for multiphase materials, composites, polymers, and nanostructures.

Acknowledgments: S.A. Syed Asif thanks AFOSR for postdoctoral support. We thank Oden Warren (Hysitron, Inc.) for helpful discussions and Paul Armistead (NRL) and Sergei Manganov (Digital Instruments) for providing samples.

[Sponsored by ONR and AFOSR]

References

[1] S.A. Syed Asif, K.J. Wahl, and R.J. Colton, "Nanoindentation and Contact Stiffness Measurement Using Force Modulation with a Capacitive Load Displacement Transducer," *Rev. Sci. Instrum.* **70**, 2408 (1999).

[2] S.A. Syed Asif, K.J. Wahl, R.J. Colton, and O.L. Warren, "Quantitative Imaging of Nanoscale Mechanical Properties Using Hybrid Nanoindentation and Force Modulation," *J. Appl. Phys.* **90**, 1192 (2001).

Raman Spectroscopy of High-Temperature Superconductors

C. Kendziora
Materials Science and Technology Division

Background: Superconductors carry current without resistive losses. This makes them very attractive for virtually any application requiring electrical power generation, distribution, or use. As the Navy moves toward the electric warship, efficient electrical power for (among other things) ship propulsion and electronic weapons will be essential, creating additional need for superconducting technology. Most of the electrical power generated today is wasted because of resistive losses. This has already driven the implementation of superconducting technology in certain niche markets, such as high-field magnets and short-distance transmission. Obstacles remaining to further enabling superconductivity include the need for low temperatures (cryogenics) as well as materials problems associated with the high-temperature superconductors based on copper and oxygen (cuprates).

Superconductivity: The mechanism of superconductivity depends on a seemingly impossible phenomenon: the attraction of electrons (or holes – the electrons' positively charged equivalent) to each other in pairs. This attractive pairing occurs despite the large coulomb repulsion the carriers feel due to their charge. Such pairs carry the "supercurrent," a "frictionless" electronic motion. Rising temperature, which accelerates electrons and shakes the crystal lattice through which they flow, tends to separate, or "break" pairs. The critical temperature (T_c)—the temperature below which superconductivity sets in—is thus dependent on the pairing strength, and ultimately on the mechanism by which the pairs form.

The cuprates have demonstrated by far the highest known T_c's—as high as 164 K, still well below room temperature (296 K). However, despite having been discovered more than 13 years ago, several fundamental principles of cuprate superconductivity remain in dispute. Ultimately, to optimize this class of materials as well as to predict superconductors with even higher T_c, we must understand how they work and, specifically, why they work so much better than anything else.

The cuprates as a material class are generally insulators. However, when extra electrons are added (or removed, for the hole-type case) through chemical substitution, they become metallic and superconducting. Through extensive study on hole-doped cuprates, a consensus has been reached in the research community that the carriers that pair in high-temperature superconductors are not only very strongly coupled, but that they possess a certain angular momentum as well, making them "*d*-wave" superconductors. This is in contrast to the elemental and alloy "conventional" superconductors that have zero angular momentum ("*s*-wave") and may be crucial for the very high T_c they achieve. Until recently, electron-doped cuprates were thought to be more "conventional" than the hole-doped cuprates and to have *s*-wave pairing. Experimentally, the pairing state can be determined by measuring the strength of the pairing as a function of direction within the crystal. As shown in Fig. 7, *s*-wave pairing is typically nearly isotropic, with no directional dependence, while *d*-wave pairing results in a characteristic anisotropy that includes "nodes," or directions where the strength is zero.

Raman Spectroscopy: Spectroscopy is the study of phenomena across some energy scale. The relevant energy scale for pairing of electrons in su-

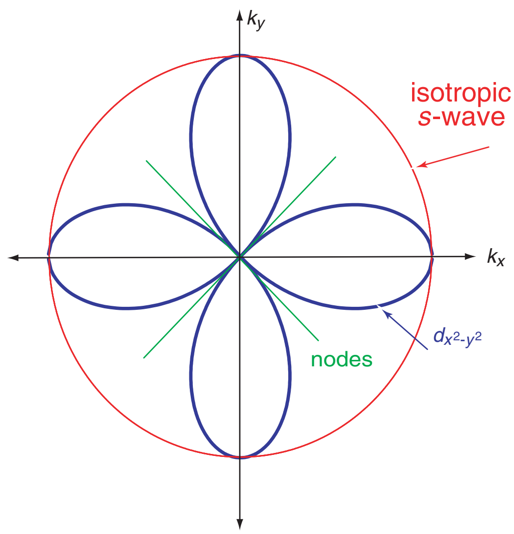

FIGURE 7
The superconducting pairing strength as a function of direction. The isotropic *s*-wave functional form (red) has no directional dependence. In contrast, the $d_{x^2-y^2}$ functional form (blue) has directions of high and low pairing strength separated by 45 deg in 4-fold symmetry.

perconductors is 0 to 0.1 eV, which is convenient for Raman spectroscopy. In the Raman process, high-energy (generally 0.5 to 3 eV) photons interact benignly with a material and produce scattered photons that have been shifted in color (energy). The number of scattered photons collected as a function of energy shift is called the Raman spectrum, and this contains unique information about both the phonon (sharp spikes) and electronic (continuum) nature of the material.

The Raman spectrum of the electron-doped cuprate $Nd_{1.85}Ce_{0.15}CuO_{4+d}$ crystal is plotted for two temperatures in Fig. 8. The incident laser energy (1.92 eV) is defined as zero, and only the downward "red" shift in energy is plotted. The red curves plot data taken at 28 K, in the normal state, while the blue curves show the Raman spectrum at 8 K in the superconducting state. As is clear in the top curve (and inset), a peak forms in the superconducting state, the energy of which (0.008 eV) is a measure of the strength of pairing. For a crystalline sample, the symmetry can be exploited using polarized photons to extract additional information. In this case, we have chosen a symmetry configuration in which no phonons are allowed and where the electronic signal is strong. Because the Raman interaction gives a weighted average of the different directions within the crystal, we cannot uniquely map out the pairing strength as a function of direction. However, we establish that the pairing is anisotropic and has nodes by the curvature of the spectrum at energies below the peak (inset). Specifically, it has the *d*-wave functional form, which predicts an intensity rise proportional to ω^3 at frequencies up to the peak.

Conclusions: The discovery of *d*-wave superconductivity in the electron-doped cuprates solved a puzzle that had troubled the high-T_c community for nearly 10 years: How can one class of materials exhibit such a high T_c via two different mechanisms? Adding the electron-doped cuprates to the class of *d*-wave superconductors allows the research community to focus on possible mechanisms for *d*-wave pairing and why this leads to such high critical temperatures. Ultimately, the goal of this undertaking is

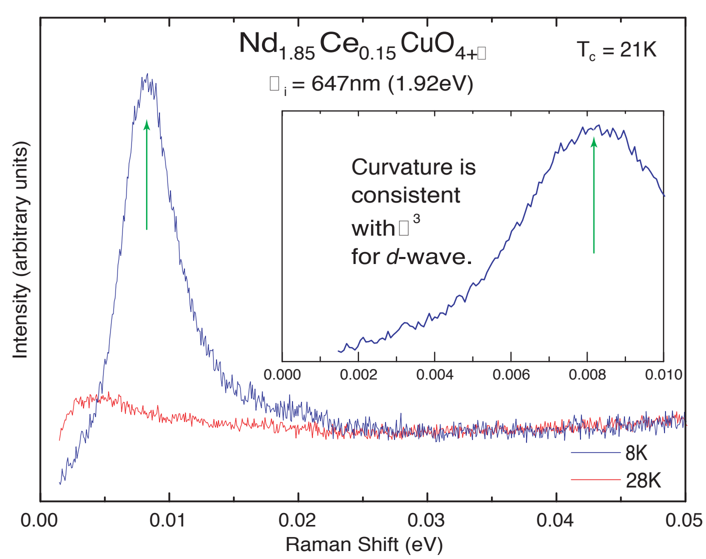

FIGURE 8
The Raman spectrum of $Nd_{1.85}Ce_{0.15}CuO_{4+d}$ measured above and below the T_c of 21K. The incident laser energy of 1.92 eV is defined as zero, and only the downward "red" shift is plotted. The inset expands the low-frequency scale for the 8 K data to accentuate the curvature.

to both raise T_c in the cuprate class of materials and to use what we have learned to predict and optimize new classes of materials with even higher critical temperatures.

Acknowledgments: Crystals were supplied by P. Fournier and R.L. Greene of the Center for Superconductivity Research and Department of Physics at the University of Maryland, College Park.

[Sponsored by ONR]

Quantum Dot Bioconjugates in Molecular Detection

J.M. Mauro, G.P. Anderson, and E.R. Goldman
Center for Bio/Molecular Science and Engineering

H. Mattoussi and B.L. Justus
Optical Sciences Division

Introduction: Fluorescent labeling of biological materials using organic dyes, especially tagging of purified antibodies, is critically important in a wide variety of diagnostic and biological imaging applications. Organic fluorophores, however, have characteristics, such as narrow excitation bands and broad red-tailing emission bands, that often limit their effectiveness. This makes concurrent resolution of multiple light-emitting probes problematic due to spectral overlap. Also, many organic dyes exhibit low resistance to photodegradation.

Luminescent colloidal semiconductor nanocrystals (quantum dots, QDs) are inorganic fluorophores that have the potential to circumvent some of the functional limitations encountered by organic dyes. In particular, CdSe-ZnS core-shell QDs exhibit size-dependent tunable photoluminescence (PL) with narrow emission bandwidths (FWHM ~ 30 to 45 nm) that span the visible spectrum and broad absorption bands. These allow simultaneous excitation of several particle sizes (colors) at a common wavelength.[1] This, in turn, allows simultaneous resolution of several colors using standard instrumentation (Fig. 9, top) . CdSe-ZnS QDs also have high quantum yields, are resistant to photodegradation, and can be detected optically at concentrations comparable to organic dyes.[2] Our effort at NRL aims to take advantage of the molecular recognition properties of antibodies in combination with the unique photophysical characteristics of QDs to provide new bioinorganic materials that can be used to detect dissolved chemicals and toxins—both natural and human-derived—within marine environments.

Meeting Our Goal: To make these novel materials, we have developed a conjugation strategy based on electrostatic interactions between negatively charged (acid-capped) CdSe-ZnS core-shell QDs and positively charged proteins.[2] Both naturally occurring and genetically engineered proteins are useful in this method, which involves simply mixing together the two charged substances (QDs and proteins) to result in self-assembled bioinorganic complexes ready for defined uses. For fluoroimmunoassays, QD-antibody conjugates can be prepared by using an adaptor protein that bridges the inorganic QD fluorophores and antibodies. Figure 9 (bottom) illustrates a mixed surface QD-conjugate consisting of two types of protein molecules surrounding a luminescent nanocrystal. Initially prepared conjugates contain both naturally occuring positively charged hen egg avidin and a variant of *E. coli* maltose binding protein (MBP-zb) engineered to have a strongly positively charged "tail" or "QD interaction domain." Biotinylated antibodies added subsequently bind tightly to the vacant biotin-binding sites of the immobilized avidin bridges, while the MBP-zb protein functions as a purification tool by allowing conjugate binding to, and elution from, solid-phase polysaccharide affinity media (this process removes any excess unbound antibodies).[3,4] Purified conjugates eluted from affinity columns can be used directly in many fluoroimmunoassays.

Figure 10 is an example of the use of the new bioconjugate materials. In this work, anti-RDX antibodies conjugated to QDs via a bridging generic antibody binding protein (protein G from *staphylococcus*) have been used to quantitate amounts of the explosive RDX (hexahydro-1,3,5-trinitro-1,3,5-triazine) dissolved in water. In the microtiter-plate based assay scheme shown (Fig. 10, top), competition between surface-immobilized and free RDX for binding to luminescent bioconjugates provides a convenient and sensitive way to monitor low levels of the explosive. Concentrations of RDX as low as 2 micrograms per liter can be detected using the present luminescent QD-conjugates.[3] Similarly sensitive assays have been developed for the explosive TNT as well as for protein toxins such as staphylococcal enterotoxin B (SEB).[4]

Many Challenges and Opportunities Remain: We have successfully taken advantage of the luminescence properties of water-soluble CdSe-ZnS quantum dots to develop simple fluorimmunoassays with detection sensitivities similar to those obtained using organic dyes. Additional assays that take ad-

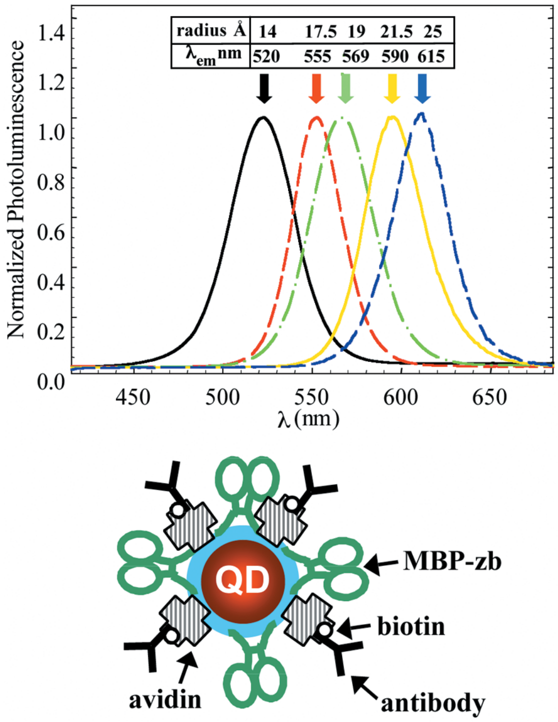

FIGURE 9
(Top) Emission spectra of a several sizes of CdSe-ZnS quantum dots, with excitation at 350 nm in all cases. (Bottom) Idealized mixed-surface QD-protein conjugate. Antibodies labeled with biotin bind efficiently to QD surfaces due to the great strength of their interaction with bridging avidin molecules.

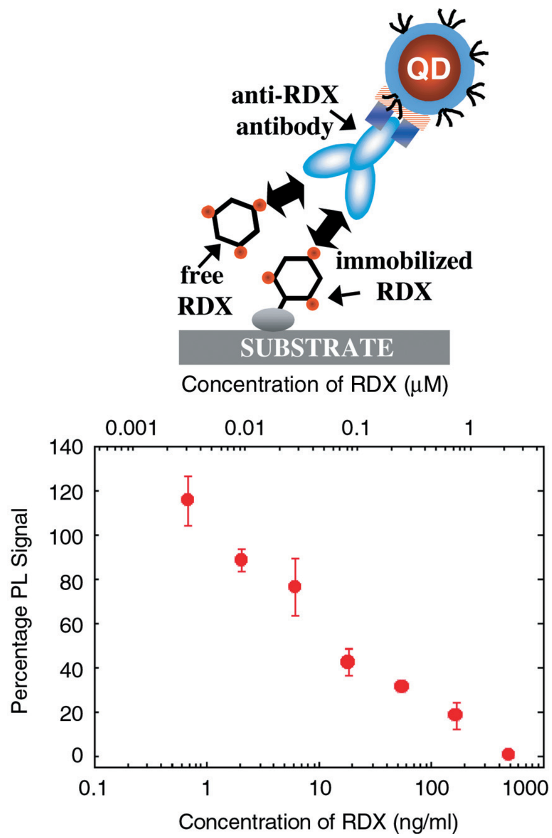

FIGURE 10
(Top) Schematic of competition-based assay for detection of low levels of dissolved RDX explosive using QD-anti-RDX antibody conjugates. (Bottom) Graphed data from competition assay, showing systematically lowered signal as increasing levels of free RDX compete with surface-immobilized RDX derivative for conjugate binding.

vantage of the unique properties of the QDs are under development. Ongoing work will exploit the novel photophysics of these semiconductor-based materials to expand the repertoire of their uses. These include simultaneous assay of several substances using multiple QD colors (multiplexed assays) as well as unique analysis methods based on quenching phenomena. Finally, using advanced microscopy methods, we are beginning to conduct experiments aimed at understanding the behavior of these nanocrystals and their bioconjugates at the single-particle level. We anticipate that fuller understanding of single-dot phenomena such as intermittent blinking, spectral shifts, effects of crystal lattice defects and surface traps, etc., and the development of other semiconductor nanocrystals with additional emission wavelengths that are not accessible with CdSe QDs will lead to development of new types of nanosensors with novel applications.

[Sponsored by ONR]

References

[1] B.O. Dabbousi, J. Rodriguez-Viejo, F.V. Mikulec, J.R. Heine, H. Mattoussi, R. Ober, K.F. Jensen, and M.G. Bawendi, "(CdSe)ZnS Core-Shell Quantum Dots: Synthesis and Characterization of a Size Series of Highly Luminescent Nanocrystallites," *J. Phys. Chem. B* **101**(46), 9463-9475 (1997).

[2] H. Mattoussi, J.M. Mauro, E.R. Goldman, G.P. Anderson, V.C. Sundar, F. Mikulec, and M.G. Bawendi, "Self-Assembly of CdSe-ZnS Quantum Dot Bioconjugates Using an Engineered Recombinant Protein," *J. Am. Chem. Soc.* **122**(49), 12142-12150 (2000).

[3] E.R. Goldman, E.D. Balighian, M.K. Kuno, S. LaBrenz, P.T. Tran, G.P. Anderson, J.M. Mauro, and H. Mattoussi, "Luminescent Quantum Dot-Adaptor Protein-Antibody Conjugates for Use in Fluoroimmunoassays," *Phys. Stat. Sol.* (in press) Jan. 2002.

[4] E.R. Goldman, G.P. Anderson, P.T. Tran, H. Mattoussi, P.T. Charles, and J.M. Mauro, "Conjugation of Luminescent Quantum Dots with Antibodies Using an Engineered Adaptor Protein Provides New Reagents for Fluoroimmunoassays," *Anal. Chem.* (in press) Jan. 2002.

Selective Resputtering-Induced Magnetic Anisotropy in High-Density Magneto-optic Media

V.G. Harris
Materials Science and Technology Division

Perpendicular Magnetic Anisotropy: Amorphous rare earth-transition metal (a-RETM) films are used as materials in magneto-optic (MO) sensors and as media for high-density MO disks. They possess perpendicular magnetic anisotropy (PMA), a unique property that allows written bits of information to align perpendicular to the plane of the storage disk. This orientation allows much higher density of information per unit area. Conventional magnetic storage media (e.g., Zip and computer hard-drive media) have bits that lie in the disk plane and therefore occupy a larger amount of space.

Discovered in 1973 by IBM researchers P. Chaudhari, J.J. Cuomo, and R.J. Gambino, these materials ushered in the modern era of high-density magneto-optic storage. To this day, they remian the industry's mainstay material. For their discovery, these authors were awarded the 1995 National Medal of Technology.[1]

Remarkably, although these materials have been used in commercial magneto-optic devices, the physical mechanism underlying their most important properties have never been made clear. In amorphous materials, unlike their more common crystalline cousins, atoms are disordered in their relative placement to each other. As such, a magnetic property that is traditionally determined by crystalline order, such as magnetic anisotropy energy that preferentially aligns the magnetization vector within a material, becomes very small. In the rare earth-containing alloys (e.g., a-TbFe), this property is often large and spontaneously aligns perpendicular to the film plane. Since the rare earth atom's shape, determined by its valence charge cloud, is nonspherical (for Tb it is more football-like), some form of local electrostatic anomaly had been proposed as the source of this property. In 1992, NRL researchers measured the presence of local atomic arrangements in a-TbFe and showed that they provide such an electrostatic anomaly and give rise to PMA via a crystal field interaction.[2] The anisotropic atomic structure is described as a statistical preference for like-atom pairs parallel to the film plane, with a corresponding preference for unlike pairs perpendicular to the plane. This preference was of the order of 5 to 8% from the ideal isotropic amorphous environment and is broadly referred to as a pair-order anisotropy (POA). Using a similar approach, we now focus our efforts to discover the growth mechanism responsible for such anisotropic atomic arrangements.

Dynamics of Film Growth in Sputter-Deposition: By examining the energy of the RF plasma used in magnetron sputtering of a-TbFe, and comparing this to the energy required to remove atoms from the growing film, deposition conditions are determined in which atoms are selectively removed from the growing film. The conditions for selective resputtering are defined in terms of a plasma energy envelope, where plasma energies between 34 eV $\leq E_{Ar} \leq$ 65 eV result in the selective removal of one specie of adatom over another from the surface of the growing film, resulting in POA.

Correlation of Atomic Structure, Plasma Energy, and Magnetic Anisotropy Energy: Extended X-ray absorption fine structure (EXAFS) measurements were performed on several films grown by using different working gas pressures (Ar gas) and RF power. These growth conditions allow for the systematic change of the plasma energy to different regions of the energy envelope, thereby allowing for an increase POA and PMA. Figure 11 plots the in-plane and out-of-plane atomic environments of Fe atoms for a subset of these samples as Fourier-transformed EXAFS data. Comparing the in-plane and out-of-plane structure clearly shows that the POA changes as a function of the RF power. In Fig. 12, the PMA is plotted with the POA as a function of Ar ion energy. A strong positive correlation exists between the Ar ion energy and both the PMA and the POA. The projection of this curve onto the three, two-dimensional planes indicates an exponential relationship between MA, POA, and Ar E, with a linear relationship between Ar E and POA.

After nearly three decades of research, both the source of PMA and the mechanism by which it is incorporated in sputtered films are now understood. This advancement will directly lead to improved processing of MO materials for sensor and media applications. Furthermore, the improved understanding of the growth dynamics of sputtered films will allow greater optimization of materials processing as well as improved understanding of the role of anisotropic atomic structure in a broad range of materials systems.

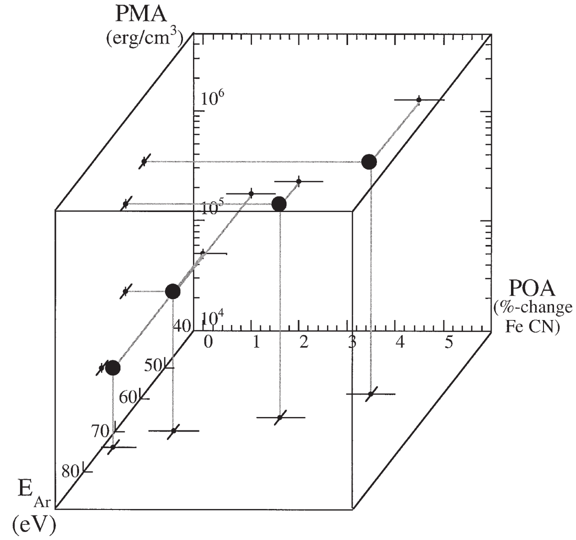

FIGURE 12
Magnetic anisotropy energy (PMA) plotted against the POA metric, with percent change in the Fe-Fe bonds between the in-plane and perpendicular directions, as a function of Ar ion energy. The data points are projected onto the two-dimensional planes illustrating the exponential relationship between the POA and the Ar E to the PMA. (From Ref. 3.)

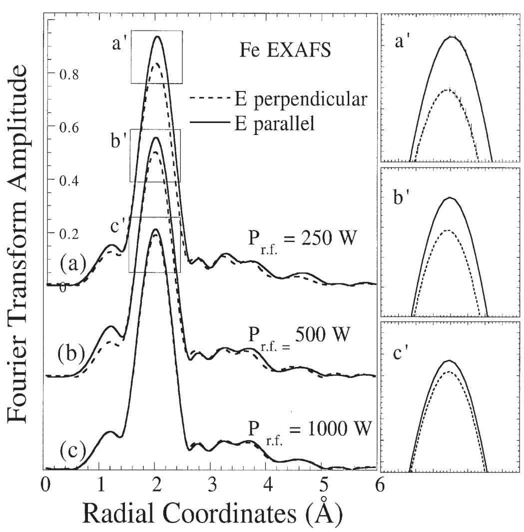

FIGURE 11
Fourier-transformed Fe EXAFS data for samples grown with increasing RF power. The amplitudes of the peaks are proportional to the occupancy and disorder while the centroid reflects the bond distance uncorrected for electron phase shift. **E** is the electric vector of the incident radiation and identifies the direction along which the structure is sampled. The atomic structural anisotropy is most evident in the near-neighbor amplitude (see insets a′, b′ and c′).(From Ref. 3.)

Acknowledgments: This work was performed in collaboration with Dr. Taras Pokhil of Seagate Technologies, Inc. (Minneapolis, MN). EXAFS measurements were performed using the Naval Research Laboratory—Synchrotron Radiation Consortium beamline X23B at the National Synchrotron Light Source (Brookhaven National Laboratory).

[Sponsored by NRL and ONR]

References

[1] http://www.ta.doc.gov/medal/

[2] V.G. Harris et al., "Structural Origins of Magnetic Anisotropy in Amorphous Tb-Fe Alloy Films," *Phys. Rev. Lett.* **69**, 1939 (1992).

[3] V.G. Harris and T. Pokhil, "Selective Resputtering Induced Perpendicular Magnetic Anisotropy in Amorphous TbFe Films," *Phys. Rev. Lett.* **87**(6), 067207 (2001).